

ABSTRACT

Title of Thesis: SUPERCONDUCTING PROPERTIES OF
THE NBN AND TIN ALLOY SYSTEM.

Abimael Santos-Cotto, Master of Science, 2019

Thesis Directed By: Dr. Christopher J.K. Richardson
Department of Materials Science

The field of quantum computation has advanced greatly in the recent years, with materials being tuned to address issues like qubit lifetime, and coherence time. Superconducting qubits based on Josephson Junctions are a promising approach for improved qubit design, yet they are made with polycrystalline and amorphous materials. Transition metal nitrides, like TiN and NbN, offer good chemical and mechanical properties as well as the possibility of a lattice matched junction, with AlN as the insulating layer. We have characterized MBE grown $\text{Nb}_x\text{Ti}_{1-x}\text{N}$ films (with $x = 0, 0.45, \text{ and } 0.78$) and a Nb₂N film by XRD and AFM. This thesis will focus on the superconducting properties: critical temperature (T_c), superconducting transition width (ΔT_c), and critical field (H_c). Two methods have been used: four-point probe DC measurements in an adiabatic demagnetization refrigerator (ADR) were used for T_c and ΔT_c measurements, and a magnetic properties measurement system (MPMS) which employs a SQUID magnetometer was employed for T_c and H_c measurements. Values of T_c ranged from 4.2 K for TiN to 15.2 K for the $x = 0.45$

film, and 14.8 for $x=0.78$, while the Nb₂N had T_c of 9.9 K, as found by DC measurements. These values agreed with those found by MPMS. The films' critical fields were found to be ~69.6 Oe for the TiN film and ~250 Oe for $x=0.78$. These results start to demonstrate the trends of the superconducting properties of alloyed Nb_xTi_{1-x}N superconductors.

SUPERCONDUCTING PROPERTIES OF THE NBN AND TIN ALLOY SYSTEM

by

Abimael Santos-Cotto

Thesis submitted to the Faculty of the Graduate School of the
University of Maryland, College Park, in partial fulfillment
of the requirements for the degree of
Master of Science
2019

Advisory Committee:

Professor Christopher J.K. Richardson, Chair
Professor John Cummings, Committee Member
Professor Ichiro Takeuchi, Committee Member

© Copyright by
Abimael Santos-Cotto
2019

Dedication

*To my mother, Rosaluz, for **absolutely everything**, besides being the best mother one could ask for. To my family, for their unconditional love and support.*

“Les amo, con todo el corazón.”

Acknowledgements

I would like to express my gratitude to everyone who, in one way or another, helped make this thesis possible; without your help these words would just be ideas.

First, I want to express my eternal gratitude to my adviser and professor, Christopher J. K. Richardson, for his guidance, everlasting patience, and unconditional support during the completion of this degree. Thank you for believing in me, for your wisdom and outstanding mentorship. Also, I'd like to thank my lab mates Chris Weddle and Ashish Alexander for their help and guidance into making resistance measurements. Moreover, thank you Austin, for growing one of the needed samples.

Additionally, I would recognize and appreciate the assistance, patience, and help, of Dr. Shanta Ranjan Saha. Without him, a big part of these pages wouldn't exist. Thank you for making time for MPMS measurements and answering my never-ending emails.

Finally, but not less important, I want to thank all the friends I've made during this time in UMD. If it weren't for all the adventures and good times, I would've certainly lost my sanity. Lastly, thank you Becca, for being my partner in crime.

Table of Contents

Dedication	ii
Acknowledgements	iii
Table of Contents	iv
List of Tables	v
List of Figures	vi
Chapter 1: Introduction and Background.....	1
1.1 Quantum Computation.....	1
1.1.1 Superconducting Qubits.....	2
1.2 Superconductivity	3
1.3 Transition Metal Nitrides.....	9
Chapter 2: Thin Film Characterization	12
2.1 Atomic Force Microscopy	12
2.2 X-Ray Diffraction	17
Chapter 3: DC Measurements.....	20
3.1 Materials and Methods.....	20
3.1.1 Measurement System.....	20
3.1.2 Sample Preparation	21
3.1.3 Measurement Procedure.....	24
3.2 DC Measurements Results.....	25
Chapter 4: MPMS Measurements.....	30
4.1 Materials and Methods.....	30
4.1.1 Measurement System.....	30
4.1.2 Sample Preparation	31
4.2 Critical Field Measurements.....	31
4.3 Critical Temperature Measurements.....	34
Chapter 5: Comparisons and Future Considerations	39
5.1 Significance and Result Summary	39
5.2 Comparison Between Measurement Systems.....	40
5.3 Future Work	41
Bibliography	43

List of Tables

2-1 Lattice parameter as determined by XRD for different $\text{Nb}_x\text{Ti}_{1-x}\text{N}$ films of varying composition	19
5-1 Summary of results.....	41

List of Figures

1-1	Superconducting magnetization curve for a type-I (left) vs type-II (right) superconductor. Field penetration begins at H_{c1} for a type-II material, lower than the thermodynamic critical field H_c	4
1-2	Current flow through a normal (left) state wire of radius R and a type-I superconducting wire (right).	6
2-1	Micrograph of the cantilever tips employed for our AFM analysis.	13
2-2	Topographical scan images for TiN, $Nb_{0.45}Ti_{0.55}N$, $Nb_{0.78}Ti_{0.22}N$, and Nb_2N thin films acquired using AFM. The scale bars on A-D are 400 nm while for E-H are 2.0 μm	15
2-3	XRD scans of the MBE grown thin films used for characterization.	17
2-4	Pole figure showing the threefold symmetry of a single crystal nitride thin film.	19
3-1	Schematic of the ADR set up used for DC measurements.	20
3-2	Schematic of the PCB board used for DC measurements.	22
3-3	Temperature vs Resistance graph of the TiN superconducting transition during DC measurements.	27
3-4	Temperature vs Resistance graph of the $Nb_{0.45}Ti_{0.55}N$ superconducting transition during DC measurements.	28
3-5	Temperature vs Resistance graph of the $Nb_{0.72}Ti_{0.28}N$ superconducting transition during DC measurements.	29
3-6	Temperature vs Resistance graph of the Nb_2N superconducting transition during DC measurements.	29

4-1	Typical setup configuration of the SQUID magnetometer inside the MPMS3. .30
4-2	MPMS critical field measurements of the TiN, Nb _{0.45} Ti _{0.55} N, and Nb _{0.72} Ti _{0.28} N films analyzed. Lower right graph shows the comparison between the three.34
4-3	MPMS Tc measurements of the TiN, Nb _{0.45} Ti _{0.55} N, and Nb _{0.72} Ti _{0.28} N films analyzed. The lower right graph shows the comparison between the three.33

Chapter 1: Introduction and Background

1.1 Quantum Computation

The modern computer has become such a common object in our lives that most of us take for granted the magical circuitry that has allowed such devices to become an integral part of the world we live in. Millions of transistors work behind the scenes turning simple electrical signals into the information nowadays shown on a screen. These signals are interpreted as “zeros” and “ones”, which form the basis of the binary system used for information processing. With the exponential miniaturization of transistors, computers are now able to carry out many operations both fast and efficiently.

There are, however, certain types of problems that are far too complicated to be solved using current digital computer algorithms; an example of this is prime factorization. During the 90’s, Peter Shor proposed an algorithm that’d be able to solve such problem using quantum computation in a fraction of the time¹. Unlike the zeros and ones in a digital computer, the state of bits in a quantum computer (QC) are in a superposition of both states. Thus, a total of 2^N classical bits are required to represent N quantum bits (qubits). These states are part of “an engineered quantum system” which are developed and built by researchers.

Various architectures are employed to create these QC components. Some worth mentioning are spin defects in materials (like the nitrogen vacancy centers in diamond)², ion traps³, topological nanowires⁴, semiconductor quantum dots⁵, and superconducting circuits⁶. However, some of the challenges faced are similar for all of

them, namely the qubit lifetime, qubit coherence time and the fidelity of coupling between multiple qubits. These crucial requirements are often, regrettably, antagonistic in nature, with systems exhibiting long coherence time are isolated and therefore exhibit weak qubit coupling and vice versa. Superconducting qubit approaches are an example of a qubit technology where the characteristics can largely be engineered. Being the focus of this research project, it is worth describing the basic principles of operation of such qubit architecture.

1.1.1 Superconducting Qubits

Qubits based on superconductors are formed by precisely designed circuits that, conceptually, can be taken as inductor-capacitor circuits with an additional component, a Josephson-Junction (JJ)⁶. There is a Josephson coupling energy between these layers that is dependent on the phase difference between them⁷. Each circuit element has then an energy associated with it:

$$E_C = \frac{1}{2}CV^2; E_L = \frac{1}{2}LI^2; E_J = I_c\Phi$$

where C is the capacitance, L is the inductance, V is the voltage across the capacitor, I is the current in the inductor, I_c is the critical current of the JJ, and Φ is the phase across the JJ. There are three main types of JJ based qubit designs: phase, charge, and flux qubits. The circuits are designed in different arrangements, yet are easily classified by their relative energies, E_C , E_L , and E_J . In the case of the phase qubit, the current density across the junction is the variable parameter; the charge is that for the charge qubit, while the magnetic flux is the parameter varied for the flux qubit⁸. When operated at temperatures approaching absolute zero, these circuits behave as quantum

mechanical oscillators, essentially artificial atoms, with allowed states that are quantized and that depend on the abovementioned variables. Benefitting from the non-linearity of the JJ, adding a degree of anharmonicity, the energy profile of these circuits can be manipulated such that the first few (ground, first, and in some cases second) states of the system can be excited without affecting higher states. One of the main challenges involved with superconducting qubits are losses due to coupling to two-level systems (TLS). The microscopic origin of these systems is unknown, but they introduce a materials dependent loss. Typically, they are observed in dielectric materials around the superconductors such as native oxides, interfacial layers, or the substrate of the thin film. TLS entities can interact with the artificial atoms, taking energy away and causing coherence times to suffer greatly.

1.2 Superconductivity

When some materials are cooled to very low temperatures, often reaching that of liquid helium, they exhibit a drastic change in their magnetic and electrical properties. Once the temperature reaches this transition point, superconductivity arises. Kamerlingh Onnes first observed such phenomenon in 1911^{9,10}. In the case of a perfect superconductor, the material will exhibit two very characteristic properties after undergoing a second order phase transition, happening at a critical temperature (T_c): perfect diamagnetism and effectively zero electrical resistance. Interestingly, in the normal state, many superconductors display less than good conductivity¹¹. The second property, perfect diamagnetism, refers to the superconductor's ability to expel any externally applied magnetic field from penetrating into it. In this chapter, some important aspects of the phenomenon of superconductivity are discussed.

Bardeen–Cooper–Schrieffer (BCS)¹² theory is a phenomenological approach to describing superconductivity and is good in explaining the Type-I superconductors. This was further expanded by Ginzburg–Landau¹³ for type-II superconductors. Type-I superconductors become normal after a sufficiently strong field is applied. Type-II superconductors on the other hand become normal in a range of magnetic fields. It begins with the magnetic field penetrating inside the SC in the form of vortices that can become pinned and interfere with the motion of electrical carriers, as shown in Figure 1-1¹⁴. Central to both theories is the concept of Cooper pairs, which are a pair of electrons formed by electron-phonon interactions that can move through the material without any scattering from lattice vibrations.

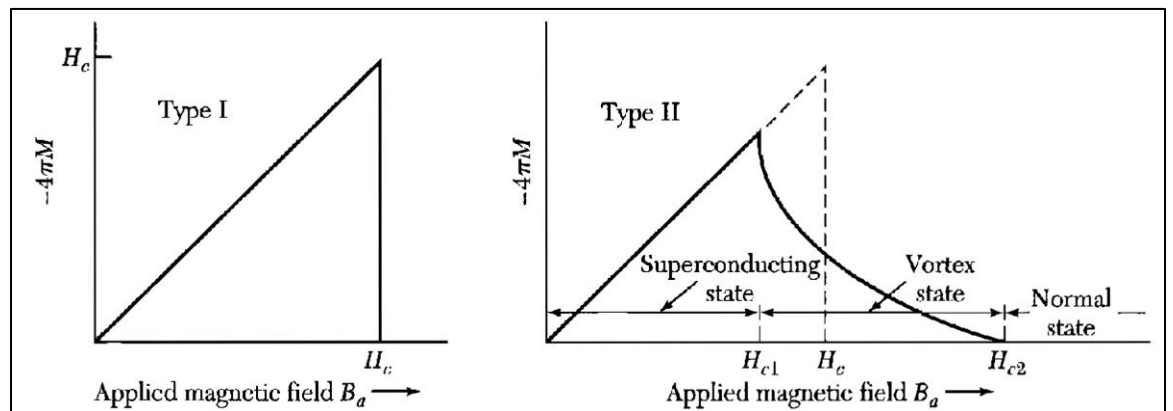


Figure 1-1: Superconducting magnetization curve for a type-I (left) vs type-II (right) superconductor. Field penetration begins at H_{c1} for a type-II material, lower than the thermodynamic critical field H_c .¹⁴

At the transition temperature, electrons condense into Cooper pairs. This occurs because at this temperature the energy of the lattice vibrations becomes less than the energy holding these electron pairs together and so, their population grows. For type-I superconductors, the sharpness in the T_c transition is a measure of the material

quality. A pure material will exhibit a more abrupt change in resistivity than one with impurities. For type-II materials this transition is never sharp.

Resistivity is known as the resistance of electrons to flow through a material due to scattering by entities ranging from phonon, impurity atoms, defects, and any other imperfection in the lattice¹¹. For metals above T_c , resistivity decreases with temperature; for insulators it increases as temperatures are lowered. Upon reaching T_c , along with a sharp drop in resistivity, there is a correspondent drop in the material's magnetic susceptibility. In many cases, the drop in resistivity will be observed before its susceptibility counterpart¹⁵. The reason behind this is that any part of the material that becomes superconductive loses its resistance and current will follow the path of least resistance. It is possible that the majority of the current to travel with negligible resistance through a small volume of the material that is superconductive.

The manifestation of diamagnetism requires more than just percolation between superconducting segments in the material. This macroscopic phenomenon, known as the Meissner effect, is a result of the generation of what are called shielding currents on the surface of the material¹⁵. On the presence of an applied magnetic field, these demagnetization currents are generated and flow around the material, creating a negative magnetic field that cancels any applied field such that there are no fields inside the material. It is worth mentioning how an applied magnetic field interacts with a superconducting medium in two instances. The first one, when the material is cooled down in the absence of a magnetic field (zero field cooling, ZFC). If after cooling to $T < T_c$, the field is turned on, the superconducting medium prevents the entrance of the applied field thanks to the generated shielding currents. The other case is that of a

superconductor being cooled while in the presence of a field (field cooling, FC). While $T > T_c$, the magnetic field lines penetrate the superconductor. When T is lowered below T_c , the same shielding currents will again expel most of the magnetic field lines from within the material. If, after cooling, the applied field is then turned off, the magnetic field lines will be trapped along the total surface of the material due to the opposing nature of the shielding currents.

Since the state of superconductivity implies that there is no loss due to material resistance, it is of interest for applications to understand then how an applied electrical current along a superconductor behaves in such. If we consider a cylindrical wire and apply a current through it, called a transport current, From Ampere's law the current will generate a magnetic field. Since there cannot be a magnetic flux going through the material, the current will only flow near the surface within a layer of finite thickness known as the London penetration depth (λ) as shown in Figure 1-2¹⁵.

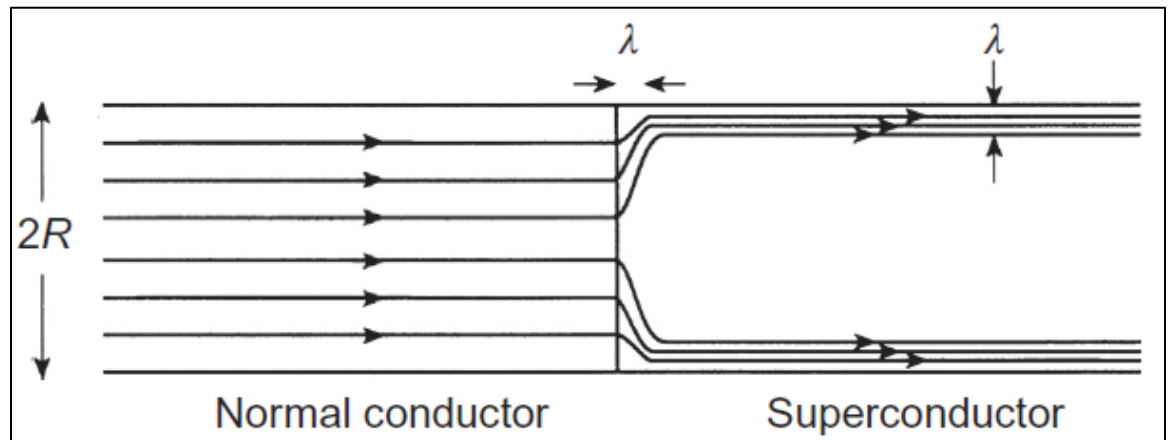


Figure 1-2 Current flow through a normal (left) state wire of radius R and a type-I superconducting wire (right).¹⁵

The London penetration depth helps describe the exponential decay of the magnetic field inside the superconductor,

$$B = B_0 \exp(-x/\lambda),$$

and

$$\lambda = \sqrt{\frac{m}{\mu n q^2}}$$

For charge carriers having mass m , charge q , and number density n . Where μ is the permeability of the material, B_0 is the magnitude of the magnetic field at the surface, and x is the distance into the superconductor from the surface.

Although a superconducting wire has many potential applications and might sound like the ultimate current carrying device, there are caveats to be considered. As previously mentioned, when T_c is reached, any magnetic field is expelled from the material as it becomes superconducting. However, a strong enough applied field will “kill” its superconductivity. The same principle applies to any supercurrent being transported through the material. When flowing, this current will induce a magnetic field which, when a sufficiently large current is transported, will also kill superconductivity. These quantities are then called the critical magnetic field and critical current. For type-I superconductors, the destruction of the superconductive state is abrupt and will cause the material to immediately return to its normal state. In the case of type-II superconductors there will be a gradual transition into the normal state known as the vortex state. When a magnetic field is strong enough to overcome the shielding currents on the material surface, the magnetic flux lines will begin penetrating it. The intensity of the field when the vortex state first begins is known as the critical

field 1 (H_{c1}), or lower critical field. As the intensity is further increased, there is a magnetic flux through the material, which has quantized values of $\frac{2\pi\hbar c}{2e}$, in the form of vortices that can be pinned. These pinned vortices appear more and more until eventually all the material returns to the normal state at the upper critical field, thus killing superconductivity. This property of type-II superconductors allows an intermediate state between absolute superconductivity and the normal state.

For characterizing the superconducting properties of our samples, we employed both a SQUID magnetometer and DC electrical measurements. We found that using the DC measurements gave us good insight into the quality of the samples prepared. Using the residual resistivity ratio (RRR) we can qualitatively assess the different structural effects such as grain boundaries and impurities and how these affect the normal state electrical resistance. In addition to determining the T_c of these samples we were able to determine how abrupt this transition was. The width of the transition gives more knowledge on whether the measured samples are type-I or type-II superconductors. We attempted to use a Quantum Designs instrument, MPMS (Magnetic Properties Measurement System) 3 which is a SQUID based magnetometer system to measure the field behavior. Our attempt to use the system was inadequate for determining the critical field yet proved useful for T_c determination therefore, most of the results presented here use DC conductivity measurements.

1.3 Transition Metal Nitrides

Throughout the literature, one can find many examples of JJ fabricated via epitaxial methods. These often involve a thin aluminum oxide layer (Al_2O_3) between two superconducting metal layers such as Al and Nb. There are, however, various challenges in using such materials. One of them is that amorphous aluminum oxide tunnel barriers have thickness variations that leads researchers to use junctions that are smaller than $1 \mu\text{m}^2$ ¹⁶. A second issue is lack of precise control of E_J leading to uncontrollable variations in the operating frequency of qubits⁶. Furthermore, the high mobility of Al at growth temperatures restricts the possibility of in situ epitaxial growth in a layer-by-layer approach¹⁷. Additional research into Nb/NbO_x/Nb JJs has shown that the oxidation of Nb results in species with multiple valence states with electrical properties ranging from insulator, semiconductor, to metallic; this also causing nonuniform-surface oxide layer^{17,18}. It might be beneficial then to design a scheme that will help reduce the involvement of such materials associated with losses. Furthermore, many of the proposed material systems suffer from poor lattice matching between the constituent parts¹⁷, which can lead to increased structural defects density on the devices, further increasing losses. With these considerations in mind, we decided to work with a different material system; that of transition metal nitrides (TmN), particularly titanium nitride (TiN), niobium nitride (NbN), and their alloys.

Titanium nitride thin films are known to have high chemical and thermal stability in addition to outstanding electrical and mechanical properties¹⁹⁻²¹. Additionally, it has shown low loss comparable to Al and Nb when employed in qubit

devices²² and a reported of $T_c \sim 6\text{K}$ ²³. Niobium nitride offers a similar improvement in operational temperature with reported T_c values reaching 16 K ²⁴ along with similar chemical and thermal stability²⁵. While these superconducting nitrides offer certain improvements over their elemental counterparts, attention to the layer material is also important. The proposed insulating material, aluminum nitride (AlN), exhibits properties such as a relatively high dielectric constant, significant thermal conductivity, along with chemical and thermal stability when employed in JJ fabrication²⁶.

As mentioned previously, many of the material designs for JJ suffer from in-plane lattice mismatch between components. The unit cell for many Tm nitrides is that of Rock Salt, while that for group III nitrides is the zinc blend, or wurtzite, unit cell²⁷. These two have comparable atomic densities per cell, with 8 atoms on each unit cell. When considering their interfacial atomic coordination, there is poor matching on their {100} planes, with mixed species appearing on the truncated surface of the rock salt structure while single species showing on the zinc blend structure. If instead we consider their {111} truncated surfaces, both structures possess single species showing coordination in this plane with a density of $\frac{4}{\sqrt{3}a^2}$ atoms-cm⁻². Particularly, the rock salt (111) plane matches with wurtzite's (0001) plane. Taking advantage of this structural compatibility we intend to fabricate a JJ with a TmN-AlN-TmN layout, with appropriate substrate selection being the first point to address.

Two substrate materials were explored as growth options for our epitaxial TmN thin films, float-zone refined Si (111) and sapphire Al₂O₃ (0001). These materials were selected because they are the only known low loss substrates that have been used in

superconducting quantum circuits. By analyzing the crystal structure of the resulting films, it was found that only TiN would preferably orient itself along the {111} planes for both substrates while NbN would only do so when grown on sapphire. More importantly, it was found that Nb reacts with Si during growth, forming Nb silicide, which is not a superconductor. Thus, following growths were done on sapphire for Tc measurements. Samples were grown using Plasma-Assisted-Molecular-Beam-Epitaxy (PAMBE) at the Laboratory for Physical Sciences. Titanium is evaporated from a high-temperature effusion cell, while niobium is evaporated from an electron gun. Nitrogen is introduced through a plasma source where the plasma decomposes the nitrogen molecule into a more reactive species of atomic nitrogen and ionized radicals.

Chapter 2: Thin Film Characterization

2.1 Atomic Force Microscopy

After growth, our samples were analyzed by various methods, among them atomic force microscopy (AFM). This microscope consists of a very small probe that has the shape of a cantilever, which in turn has an even smaller tip emerging from its free side; the probe is often made from piezoelectric materials. Focused on this probe is a laser beam that is reflected to a four-quadrant photodiode, which detects deviations in the position of the tip as the scanner mechanism passes it over the sample. The tool operates mainly in two modes: contact and non-contact mode. In the first, the tip is scanned across the surface while “touching” the sample, acquiring information of the various forces interacting with the tip. In the latter, the tip is vertically oscillated close to its resonant frequency while scanned near the surface, providing topography measurements of the sample. This non-contact mode is sometimes referred to as “tapping mode”. In addition to topography, by tracking shifts in the tip’s oscillation phase, areas of the sample with varying materials can be identified. The whole mechanism is modulated by a feedback loop that keeps the distance, the oscillation amplitude on tapping mode, or force, during contact mode, between the tip and sample constant.

For our samples, we employed a “Bruker Dimension Icon with Scan Assist” which is maintained at LPS. The instrument allows for wafers of up to 6 inches to be analyzed. It has a scanning range, in the non-vertical X-Y directions, of up to 90 μm x 90 μm while allowing for up to 10 μm in the vertical range (Z direction). The instrument

was used in non-contact “tapping” mode, which offers lateral resolution between 1-5 nm for most samples, better than contact mode. At the same time, using “tapping mode” eliminates unnecessary forces to be exerted on the tip which avoids wear and tear on them. The cantilever tips used are manufactured by TED Pella, Inc.; their model TAP300AL-G, shown in Figure 2-1. These tips are designed specifically for intermittent contact and perfect for tapping mode.



*Figure 2-1 Micrograph of the cantilever tips employed for our AFM analysis.
https://www.tedpella.com/probes_html/bstap300.jpg*

Additionally they have a 30-nm Al coating on their flat surface opposite side of tip for enhanced laser reflectivity. The tip has a radius of < 10 nm, a height of $17 \mu\text{m}$, and a cantilever length, width and thickness of 125 , 30 , and $4 \mu\text{m}$, respectively. The probe’s resonant frequency is 300 kHz and has a force constant of 40 N/m.

For all of our samples, 1:1 aspect ratio images of $2\text{-}\mu\text{m}$ and $10\text{-}\mu\text{m}$ sizes were acquired. Initially, fast scan rates and lower resolution are used to make a topography assesment prior to image acquisition. Then, settings are fine tuned to improve image quality. To increase the resolution and quality of these images, at the expense of longer scan times, a 1008 sample points and line were taken. Depending on the observed topography, scan rates were varied, ranging from $0.496\text{-}0.855$ Hz. In addition to scan rate, two other parameters are optimized, the integral and proportional gains. These are scaling factors applied to the error signal in the feedback loop that determine how fast corrections to the oscillation amplitude must be made in order to keep it constant. If

the integral gain, the scaling factor applied to the average error signal, is too low, rough surfaces will show poor trace and retrace signals, this because the tip's response to topography changes is too slow. On the other hand, if set too high, noisy trace/retrace signals are obtained, leading to image artifacts. The proportional gain, the scaling factor proportional to the error signal, is often optimized after the integral gain.

Upon acquisition, images were analyzed using the software provided with the AFM instrument, NanoScope Analysis v1.9. Images were first flattened to varying degrees, depending on scan size. The main aspects to study were the sample's surface roughness and type of topography. Figure 2-2 shows the the topographical scan images for samples D2G0139, D2G0140, D2G0141, and D2G0154; these are respectively TiN, Nb_{0.45}Ti_{0.55}N, Nb_{0.72}Ti_{0.28}N, and Nb₂N. The films' thicknesses are 45, 205, 88, and 37 nm, respectively. The top row images (A-D) are 2- μ m scans for the aforementioned samples, while images E-H are 10- μ m scans. The scale bars on A-D is 400 nm while the E-H ones are 2.0 μ m. The TiN sample exhibited a surface roughness of 1.16 nm and 1.35 nm for the 2- μ m and 10- μ m scans. Sample Nb_{0.45}Ti_{0.55}N, as can be seen, is rougher with values of 8.84 nm (2- μ m) and 9.85 nm (10- μ m), and that of Nb_{0.72}Ti_{0.28}N with roughness values of 1.72 nm (2- μ m) and 1.76 nm (10- μ m). Finally, the Nb₂N sample had a surface roughness of 4.33 nm (2- μ m) and 5.22 nm (10- μ m).

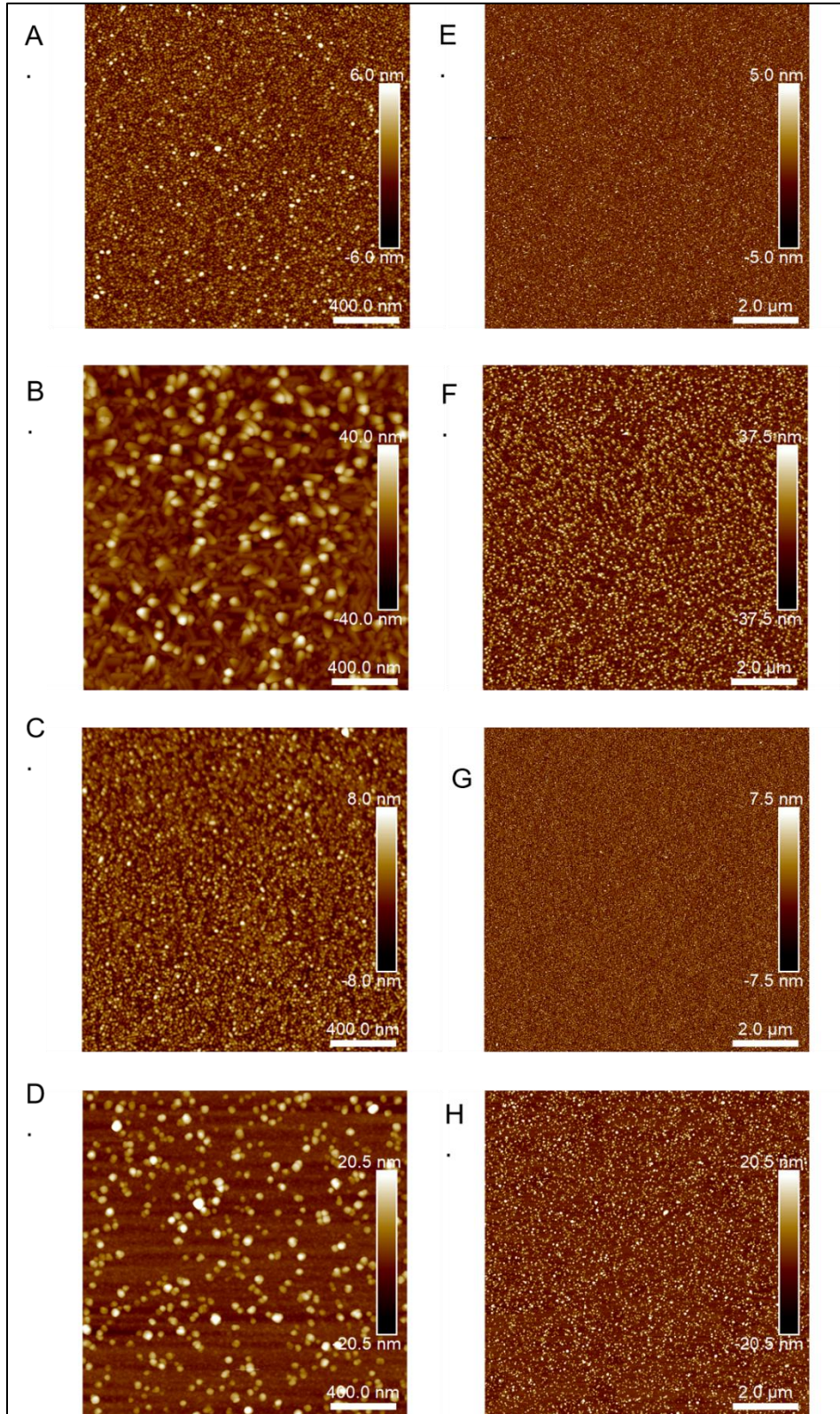


Figure 2-2 Topographical scan images for TiN, $Nb_{0.45}Ti_{0.55}N$, $Nb_{0.78}Ti_{0.22}N$, and Nb_2N thin films acquired using AFM. The scale bars on A-D are 400 nm while for E-H are 2.0 μm

The river rock topography observed is consistent with nitrogen rich growth conditions. On scan B, it is observed that the topography resulted from 3D mounded growth mode. Surface roughness is governed by the kinetics involved in the growing process and thus it is the growing parameters that will ultimately control this value. It is, however, desirable to obtain the smoothest surface on our films if they are to be used for JJ since any surface variations could lead to deterioration of the JJ performance, or lack of performance in general.

2.2 X-Ray Diffraction

Perhaps one of the most insightful tools for characterizing epitaxial materials is X-ray crystallography. In this technique, a source generates X-ray radiation of a particular wavelength and this beam is then diffracted by the sample as described by Bragg's law,

$$2d\sin\theta = n\lambda$$

which dictates requirements for diffraction to happen for a given atomic plane spacing, d , where θ is the angle between the incident beam and the crystallographic plane, λ is the wavelength of the incident beam at the sample, and n is the diffraction order. For this we utilized a PANalytical X'Pert PRO X-ray diffractometer with a Cu $K\alpha$ source, $\lambda = 0.15406$ nm.

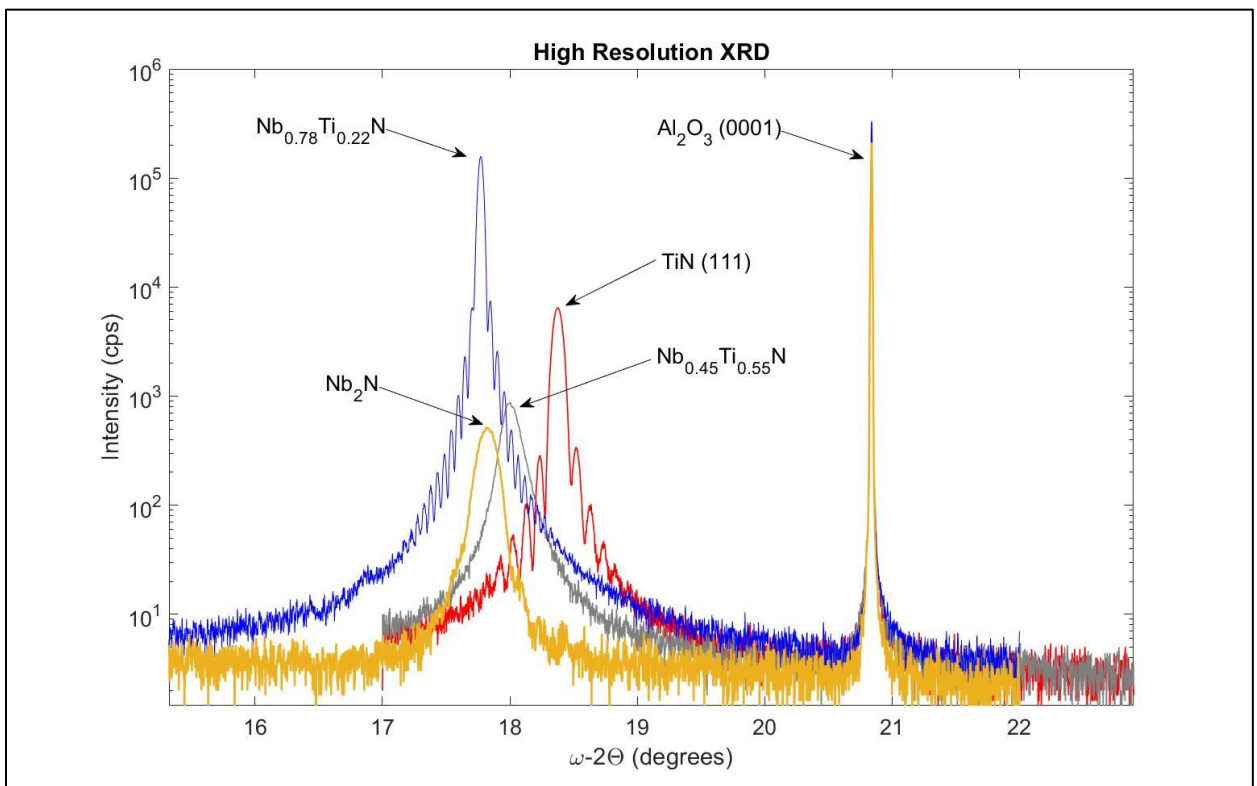


Figure 2-3 XRD scans of the MBE grown thin films used for characterization.

Figure 2-3 shows a high resolution XRD scan for the peaks of interest of our samples. The lattice parameter for pure TiN and NbN are 0.423 and 0.443 nm, respectively, as shown in the table below^{28,29}. Using the lever rule between these two compounds and their lattice parameters one can then determine the composition of the resulting alloys between these two compounds. These should, naturally, lie between the tie line points. By observing the Nb₂N and Nb_{0.72}Ti_{0.28}N peaks on the XRD figure it is evident that the peak labeled “Nb₂N” is further right than the mentioned alloy. Further study has found that this sample is, actually, hexagonal Nb₂N. At the time of this version the proper growth parameters needed to grow rock salt NbN have not been determined. From the XRD peaks one can determine the type of material present; if in addition to our main peaks one could find smaller peaks, it could be evidence of smaller phases growing on the film in conjunction with our desired compound. Using a different type of scan, one can determine the crystallinity of the sample. The generation of what is known as a pole figure will allow to determine whether the film in question is a single crystal or if it is polycrystalline. Figure 2-4 shows an example of a pole figure for a single crystal (111) cubic niobium nitride film with threefold symmetry around the [111] growth direction that was grown in our MBE lab. If the film were polycrystalline, the resulting figure would have a band of intensity instead of three sharp distinctive ones.

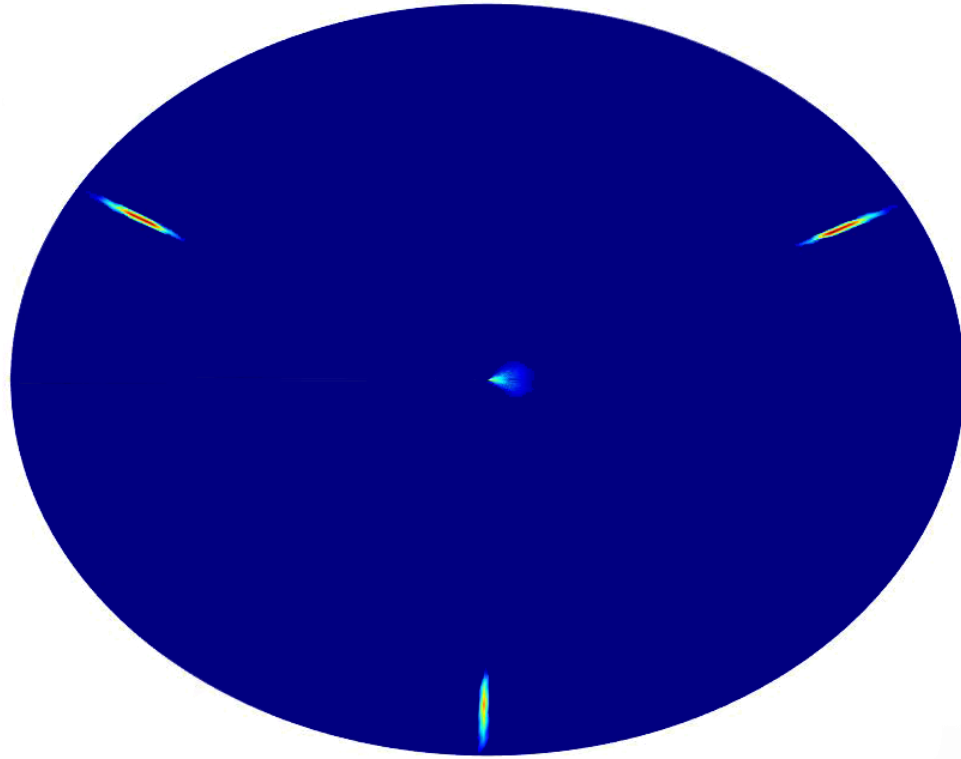


Figure 2-4 Pole figure showing the threefold symmetry of a single crystal nitride thin film.

Table 2-1 Lattice parameter a as determined by XRD for different $Nb_xTi_{1-x}N$ films of varying composition.

Compound	Lattice Parameter a (nm)
TiN	0.423
$Nb_{0.45}Ti_{0.55}N$	0.432
$Nb_{0.78}Ti_{0.22}N$	0.437
NbN	0.443
Nb_2N^{30}	0.303

Chapter 3: DC Measurements

3.1 Materials and Methods

3.1.1 Measurement System

DC measurements were made at the 4 Kelvin stage inside of an adiabatic demagnetization refrigerator (ADR), manufactured by High Precision Devices. The ADR consists of four temperature stages, each nested inside the other with varying shielding materials as shown in Figure 3-1. The outer stage, at room temperature, consists of a vacuum shroud separated inside by a lightweight metal which encloses the 50 K stage. Inside this, a radiative shield allows temperatures to reach 4 K, where our samples are located. The remaining stages, which are not used for our DC measurements, are shielded by Mu metal and a Cu Radiative shield and allow temperatures to reach 50 mK. The vacuum in the ADR is generated initially by a Pfeiffer Vacuum turbo pump in line with a roughing pump, lowering the pressure to the $\sim 10^{-8}$ Torr range.

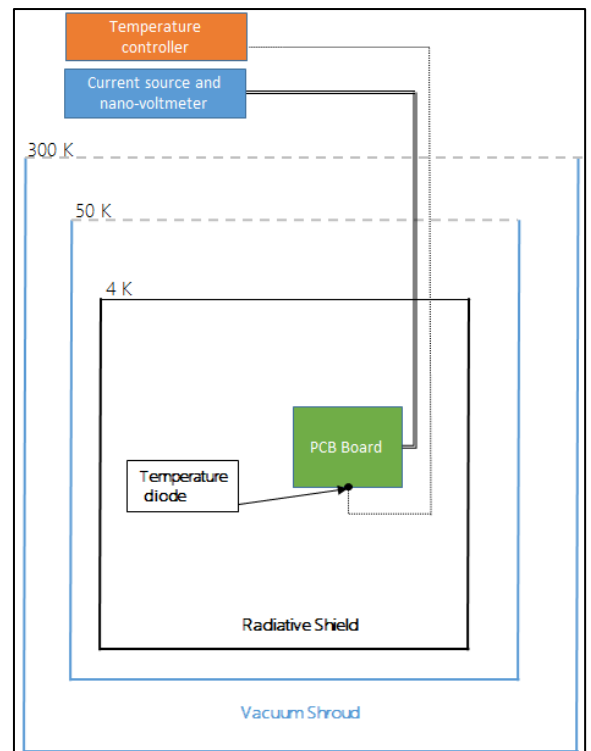


Figure 3-1 Schematic of the ADR set up used for DC measurements.

3.1.2 Sample Preparation

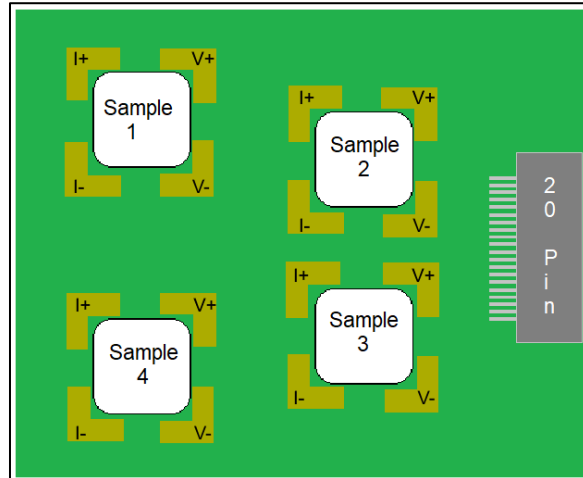
To conduct our DC measurements, our samples had to be fitted into our ADR system. This multi-step process included dicing of the samples, preparation of the PCB board where the samples would be connected to, wire bonding of the samples, in addition to fabrication of custom wiring to perform our measurements. After AFM and XRD measurements, the samples are then spin coated with a layer of OiR 906-10 resist. The idea is to protect the samples from mechanical damage during the dicing procedure. Subsequently, an adhesive “dicing tape” is affixed to the back of the wafers. The tape’s purpose is to improve the contact between the wafer and the dicing saw’s chuck, which holds the samples in place by producing a small vacuum. It is recommended that after taping the samples they’re allowed to rest for a few hours to improve adhesion during dicing. Otherwise, if small pieces are desired, these might fly away during dicing, causing samples to be loss within the dicing saw.

Disco Corporation manufactures the dicing saw used, model DAD3220. For our sapphire wafers, a diamond blade of type CA-010-270-080-H with a thickness of 0.257 mm is used. The recipe to dice sapphire, a very hard materials, a slow feed speed 0.75 mm /s is used with a 22,000-RPM spindle rotation. Given the size limitations for both the PCB board and MPMS measurements, the die dimensions were chosen to be 3.5 mm X 3.5 mm. After dicing, the tape was removed from the samples and the resist coating was dissolved away with acetone, with a subsequent wash with methanol, and finally isopropyl alcohol.

Following dicing, the square samples were adhered to a copper plate, which works both as a support for the PCB and samples and as a thermal conductor to ensure

proper cooling. Adhesion was done using GE Varnish (VGE-7031) that was thermally cured at 140°C. The varnish is manufactured by LakeShore Cryotronics and is specially designed for cryogenic applications. It exhibits good chemical resistance, fast tack time and bonding versatility. Additionally, it supports vacuum applications with pressures as low as 9.98×10^{-9} Torr without any outgassing. Furthermore, it enhances thermal contact while offering an electrically insulating layer at low temperatures. After curing, the PCB board was screwed to the copper plate for wire bonding.

The PCB boards used were designed at LPS and custom made by Bay Area Circuits. They have a 4-wire per sample configuration with up to four samples per board, as seen in Figure 3-2. The 4-wire connectors on the sample holders had solder covering the copper contacts, which was not removable using normal de-soldering



techniques. To remove said layer, the contacts were first brushed with a carbon steel brush using a Dremel tool at medium speed, removing excess material. After that, sanding using 1000, 3000 and 7000 grit paper was done until a considerably reflective copper surface was obtained. Despite the smoothness of the surface, it was necessary to perform a brief re-sanding with 7000 grit paper using isopropyl alcohol as a lubricant, instead of water, before the wire bonding process. Following sanding, the PCB board was rinsed with alcohol, dried with N₂ gas, and attached to the copper plate

Figure 3-2 Schematic of the PCB board used for DC measurements.

contacts were first brushed with a carbon steel brush using a Dremel tool at medium speed, removing excess material. After that, sanding using 1000, 3000 and 7000 grit paper was done until a considerably reflective copper surface was obtained. Despite the smoothness of the surface, it was necessary to perform a brief re-sanding with 7000 grit paper using isopropyl alcohol as a lubricant, instead of water, before the wire bonding process. Following sanding, the PCB board was rinsed with alcohol, dried with N₂ gas, and attached to the copper plate

with the samples. For wire bonding, we employed a West-Bond Wire-Bonder, model no. 7476E-79, which is a wedge-wedge manual bonder. The wire is threaded to a metal capillary with a wedged tip under which the wire is placed. Upon contacting the surface, a transducer generates an ultrasonic pulse through the tip, effectively bonding the wire to the surface. The wire used is a 1:99 Si/Al alloy with 25- μm diameter.

After bonding the samples to the PCB board, a 20-pin connector is soldered and secured to the board, of which only 16 pins were used. Kapton® insulated wires leading were used to make electrical connections. This type of wiring was used due to its suitability for ultra-high vacuum ($1\text{e-}10$ Torr) and cryogenic environments (-273 °C). The four connectors on each of the samples were set to perform a 4-point-probe measurement type. In order to obtain the best results, two measurement configurations were attempted and the resistance across the samples measured; one with horizontal current flow and the other with vertical current flow. It was found that the vertical current flow configuration exhibited the least resistance, allowing for more accurate measurements.

In addition to our samples, a Lakeshore DTS-670SD silicon temperature diode with a 4-point-probe configuration was included in the 25-pin connector. A cryoloom from LakeShore is used to conduct the signals to the room temperature vacuum feedthrough on the top of the ADR. On the exterior part, the wiring leads to a connection box with BNC cable inputs which are used for the sample measurements while the temperature sensor wires lead to a Stanford Research Instruments 922 (SRS-922) unit for temperature data acquisition. The BNC cables lead to a Keithley 6220 Precision Current Source and a Keithley 2182A Nanovoltmeter. The combination of

these instruments enables measurements of resistance down to the micro-ohm range with an average noise floor of $4.467 \mu\Omega$. These instruments, in turn, are connected via a GPIB interface connection and are controlled through MATLAB scripts.

This sample setup was attached to a thicker copper plate which contains a hole to hold the temperature sensor. Prior to introducing the temperature sensor, the hole was filled with Apiezon N grease. Said grease is recommended for cryogenic and high vacuum applications given its low vapor pressure and outgassing, thermal conductivity, and its ability to withstand frequent thermal cycling (-273 to $+30$ °C) without crazing. Additionally, it is easily pliable at room temperature, while solidifying at low temperatures, providing good mounting support for the sensor. In turn, the entire sample setup, samples and temperature diode, is attached to the 4 K stage of our ADR system.

3.1.3 Measurement Procedure

After ADR closure, the cooling cycle starts and cooldown measurements are made for one sample at a time, given instrumental limitations. By observing the behavior of the temperature vs. resistance curve, some insight into whether the material behaves like an insulator or a metal is obtained. The former is characterized by an incremental resistance as temperatures are lowered while the latter exhibits lower resistances as temperatures reach that of the superconducting state. Upon transition, resistance drops sharply, yet a measurable transition width can be observed. Since cooldowns usually take ~15 hours for temperatures to drop from room temperature (~293 K) to 3 K, measurement intervals are longer and so the resolution of the transition width is not ideal. For this reason, a short warmup measurement (3 ~ 20 K) is made

with 1 second measurement intervals, which allows not only for better resolution (0.007 K), but for a more accurate determination of the T_c and ΔT_c . T_c was selected as the temperature point at which the material's resistance becomes negligible, i.e. the last point on the resistance drop, right before it stabilizes in the micro/nano-ohm range. For ΔT_c , the upper temperature was taken as the point at which the resistance is 90% of the normal state resistance in the T vs. R graphs, while the lower point was T_c . To determine the uncertainty of the transition width, the point just above the determined temperature for 90% resistance was averaged with said 90% resistance T value, and their differences were taken. On the lower end, at T_c , the same procedure was taken, yet with the point just below T_c since given the abrupt change in resistance. As an example, for $Nb_{0.45}Ti_{0.55}N$, ΔT_c is calculated as follows: the normal state resistance before T_c was 1.29 Ohms at 15.6 K; taking 90% of that leads us to $T=15.42$ K with the upper point being 15.43 K, so $\delta=0.006$ K and $\langle \text{avg} \rangle = 15.43$ K. With a similar procedure at the lower T (15.25- 15.22 K), leads to $\delta=0.032$ and $\langle \text{avg} \rangle=15.24$ K. The final transition width is then 0.19 K with an error of ± 0.04 K. There is an additional source of uncertainty, which is the repeatability. Since these measurements were only conducted once, the uncertainty is unknown.

3.2 DC Measurements Results

The data presented is for three samples, namely TiN, $Nb_{0.45}Ti_{0.55}N$, $Nb_{0.78}Ti_{0.22}N$ and Nb_2N . By observing the behavior of the resistance as the temperature drops, the material can be identified as having an insulating or metallic behavior. If resistance increases as T goes down, the material behaves as an insulator, while if it

drops, it has a metallic behavior. This metallic behavior arises due to the reduced thermal vibrations in the material being measured which in turn cause less electron scattering, thus improving conduction. Another important figure of merit obtainable from these graphs is the residual-resistance-ratio (RRR) for the material. This is the ratio of the film's resistance at room temperature to the resistance at T just above T_c . This provides insight into the quality of the material. A high RRR is expected for a material with a metallic behavior, in which resistance is proportional to the temperature, whereas a low RRR is expected from insulating materials. Impurities, grain boundaries, and the crystallinity of the material will be reflected by its RRR. Figure 3-3 shows the superconductive transition of a TiN film of 45 nm thickness. The transition temperature is 4.2 K with a transition width (ΔT_c) of 0.03 K and a RRR of 1.78, exhibiting a metallic behavior. The T_c obtained for this sample agrees with values reported in the literature. Lefloch et al³¹ reported a T_c for a 100 nm TiN film of 4.6 K, yet values up to 6 K³² have also been reported in the literature.

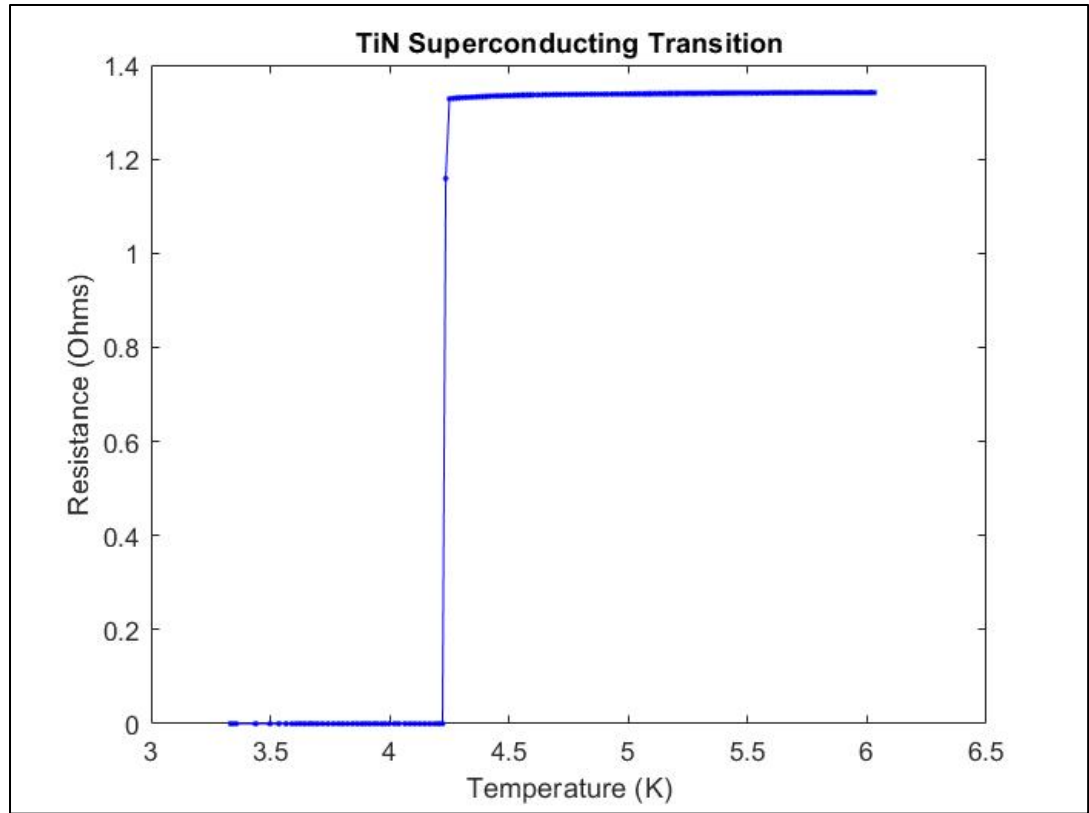


Figure 3-3 Temperature vs Resistance graph of the TiN superconducting transition during DC measurements.

Figure 3-4, left, shows the superconducting transition for $\text{Nb}_{0.45}\text{Ti}_{0.55}\text{N}$. The T_c is 15.2 K and the ΔT_c is 0.2 K. Figure 3-4 right shows the T vs R behavior for said sample throughout the whole cooldown. As can be observed, it has a metallic behavior, and a $\text{RRR}(\text{RT}/16\text{K})$ of 1.19. For similar alloy fractions, literature reports T_c values between 15.2 and 15.5 K³³.

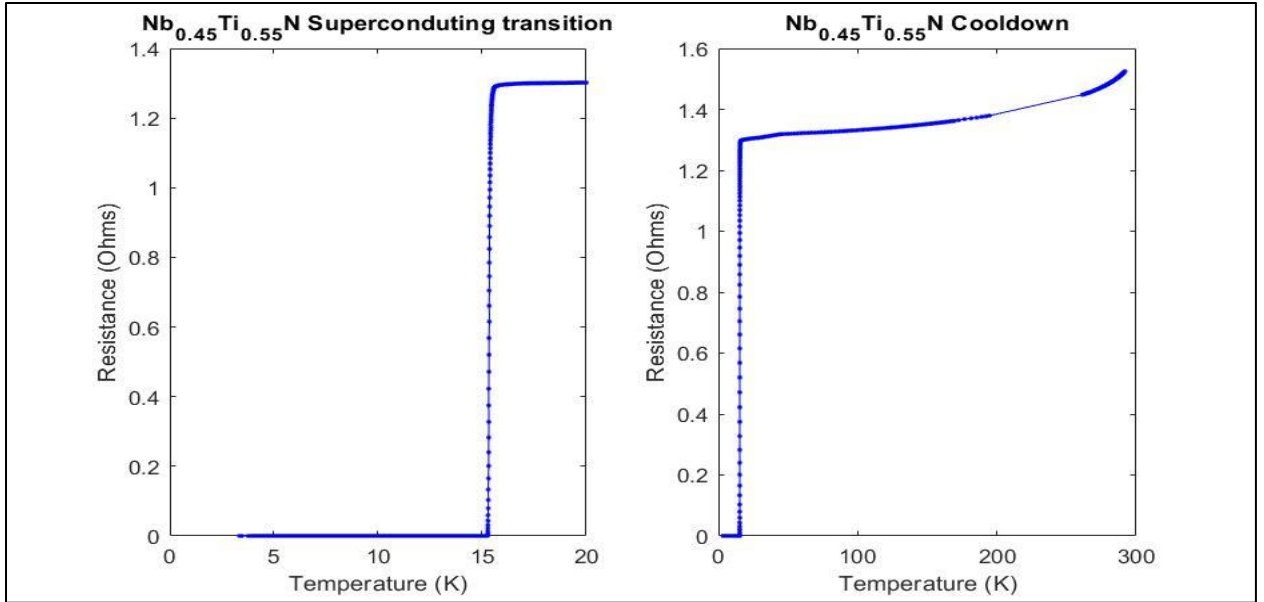


Figure 3-4 Temperature vs Resistance graph of the $Nb_{0.45}Ti_{0.55}N$ superconducting transition during DC measurements.

Figure 3-5 shows the superconducting transition for $Nb_{0.72}Ti_{0.28}N$. The T_c for this film was 14.8 K and the ΔT_c was 0.23 K. Unlike TiN and the $Nb_{0.45}Ti_{0.55}N$ sample, this film behaved more like an insulating material. It exhibited a RRR (RT/15.7 K) of 0.84. Literature reports values for T_c of 14.5 K for similar alloy fractions, which agree with our findings^{34,35}.

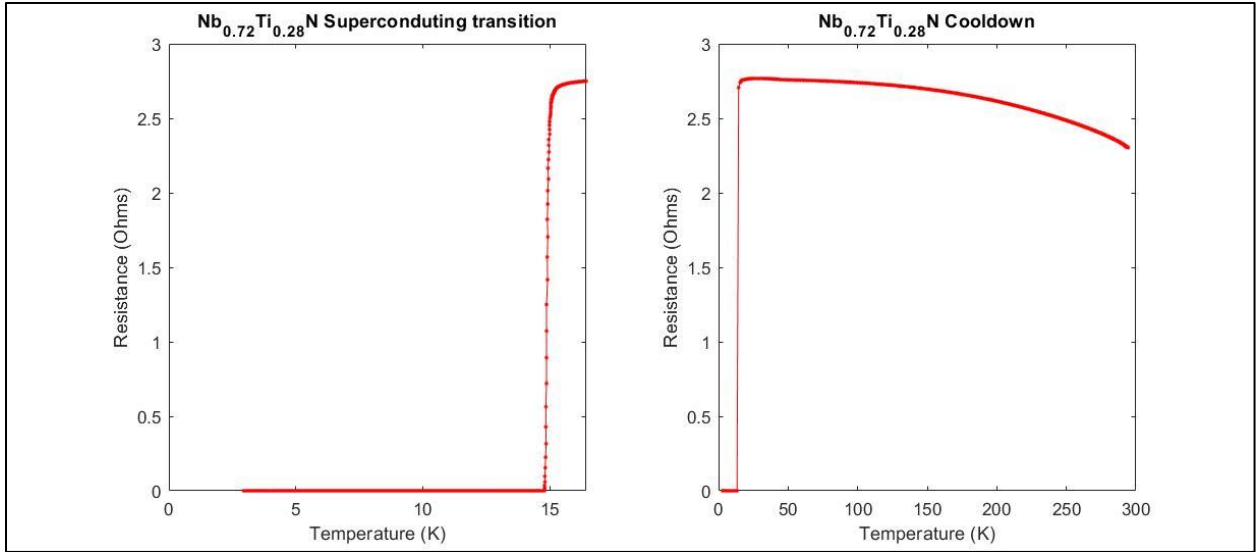


Figure 3 Temperature vs Resistance graph of the $Nb_{0.72}Ti_{0.28}N$ superconducting transition during DC measurements.

Figure 3-6 shows the superconducting transition for pure Nb_2N with a T_c of 9.9 K and a ΔT_c of 0.26 K. The RRR for this sample was 0.50, exhibiting an insulating behavior. The measured T_c is close to that reported of other studies of T_c being close to 10 K³⁶.

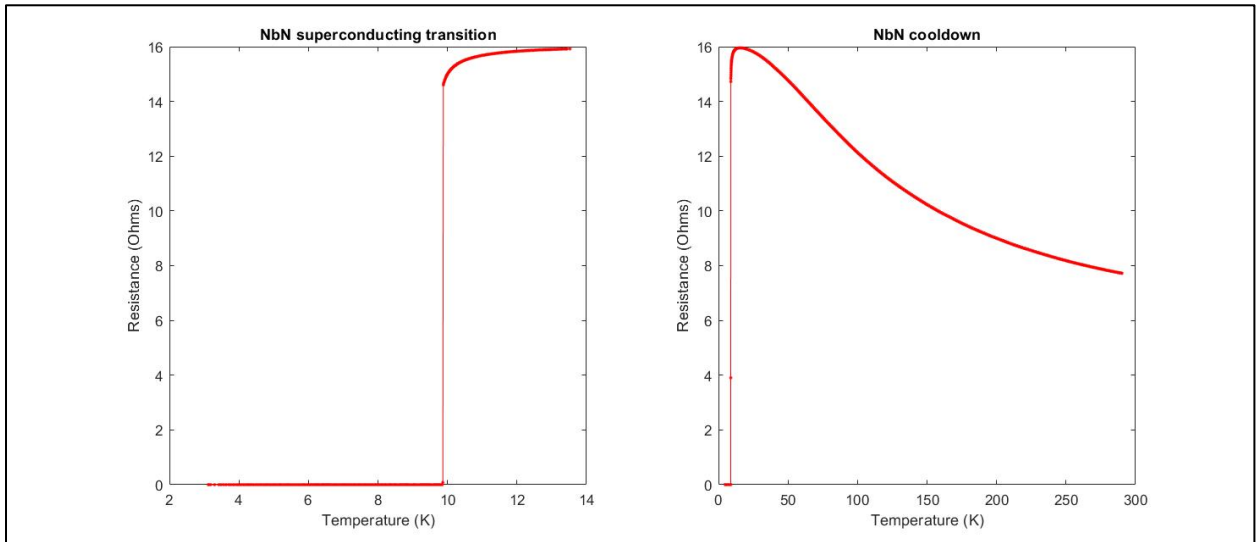


Figure 3-6 Temperature vs Resistance graph of the Nb_2N superconducting transition during DC measurements.

Chapter 4: MPMS Measurements

4.1 Materials and Methods

4.1.1 Measurement System

As mentioned before, the magnetic properties of our samples were studied using a MPMS 3 instrument that is maintained in the UMD Center for Nanophysics and Advanced Materials. This instrument allows for extremely sensitive measurements of changes in magnetic moment. It employs a second-order gradiometer in the form of two pickup coils which are counter-wound as seen in figure 4-1³⁷. These coils are connected to a SQUID (superconducting quantum interference device) detector which, using two JJ's in parallel, can detect very small variations in magnetic fields. The instrument works by passing a sample through these metal coils. Given the

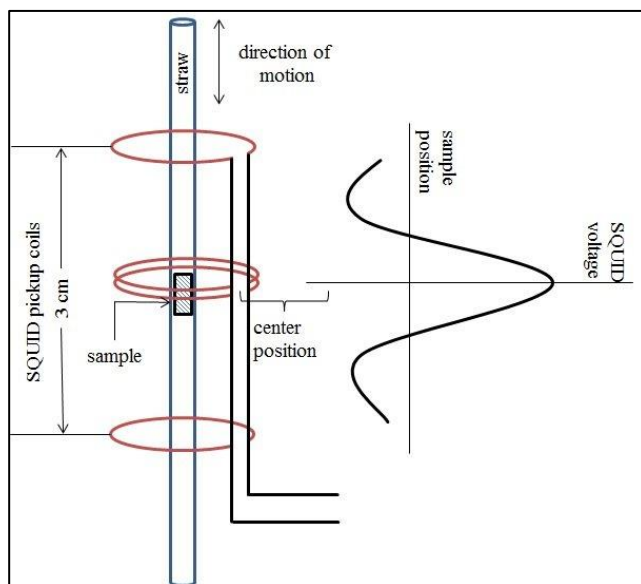


Figure 4-1 Typical setup configuration of the SQUID magnetometer inside the MPMS3.³⁷

magnetic signature for a given sample, as it passes through the detection coils, their magnetic field will induce a small current along the coil, which will produce a voltage change on the SQUID, which is then converted into magnetic moment units. The MPMS allows for samples to be studied at temperatures ranging from 1.8 K to 400 K. with a sensitivity of 10^{-8} emu. Additionally, samples can be submitted to magnetic

fields up to 7 Tesla using the MPMS 3, allowing for both T_c and H_c analysis in the case of our samples.

4.1.2 Sample Preparation

For the MPMS 3 measurements, samples were used as previously diced, i.e. 3.5 x 3.5 mm in size. A plastic straw, of the same kind used for beverages, is cut in half and sliced through its cross section on one of the sides such that the diameter can be reduced. To one of these halves, a small strip of Kapton® tape attached as to create a surface to place the sample. The sample is then placed on top of the tape, with its surface perpendicular to the length of the straw. Then, a second strip of tape is placed on top of the sample to secure it in place. Afterwards, this straw half is slid through another, uncut, straw. Care is taken to place the sample at the center position of the sample setup. For this, Quantum Design provides a metal guide that shows the position the sample would have inside the instrument. Once the sample is properly placed, the second sliced straw half is inserted through the top part of the uncut straw. Finally, this whole setup is attached to an adapter and then to the instruments sample holder that places it inside the MPMS 3. The reason to use plastic straw as a sample holder is that it possesses a negligible magnetic signature, thus minimizing any noise or false readings during measurements.

4.2 Critical Field Measurements

As previously mentioned, a sufficiently strong magnetic field can destroy superconductivity in a material. This happens when the applied magnetic field overcomes the effect of the shielding currents on the superconductor's surface and

magnetic flux lines penetrate inside it. For type-I superconductors, this destruction of superconductivity is immediate once a sufficiently strong field is applied. However, for type-II superconductors, there is an upper and lower limit for this critical field, namely H_{c1} and H_{c2} . The lower limit is that when magnetic flux lines start penetrating the material, and as this happens, regions within the material return to the normal state. As the density of these vortex state lines increases, the superconducting properties continue to diminish until, at H_{c2} , superconductivity is effectively destroyed and all the magnetic field penetrates the material, forcing it into the normal state. Just as a strong enough applied field can cause this effect, a sufficiently strong supercurrent (a critical current) will induce a strong magnetic field and kill superconductivity. This last property is commonly exploited for the generation of very strong magnetic fields without the need of great power inputs since a supercurrent can be easily maintained within a superconducting ring.

Using the MPMS 3 tool, in addition to T_c measurements, we intended to determine the critical field for our sample films. Commonly, the process involves keeping the sample at a constant temperature below T_c and measuring its magnetic moment response as a varying magnetic field is applied. For our measurements, the samples were kept at 2 K while the field was varied between 0 to 1 T (10,000 Oe), lowered again to 0 and increased to -1 T (-10,000 Oe) and then zeroed again. The expected graph resembles that of TiN and $Nb_{0.78}Ti_{0.22}N$, as seen in Figure 4-2, yet should be significantly less noisy. The data for $Nb_{0.45}Ti_{0.55}N$ was, regrettably, not useful at all. Given the noisy data, an accurate determination of H_{c1} is hard and is prone to errors and so the following values are approximations; for TiN, the magnetic flux

penetration seems to begin at ~ 69.6 Oe. In the case of the Hc2, for both -1 T and 1 T, superconductivity seems to vanish at $\sim \pm 9000$ Oe, or 0.9 T. For the Nb_{0.78}Ti_{0.22}N sample, Hc1 appears around 250 Oe. For this sample, although the graph is evidently continuous at large fields, it might be a result of the measurement parameters, and so it is very plausible that there should be a discontinuity at the extremes of this curve. Thus, it shows that the Hc2 for this NbTiN sample exceeds 1 T. It is evident that the obtained data, although having the proper general behavior, is noisy.

While the exact reasons for this are unclear, it is possible that, given the thin film nature of our samples, the quality of the signal obtained was affected by substrate contributions of the titanium layer on the back side. In the case of the Nb_{0.45}Ti_{0.55}N sample, there is no known reason as of why the data was completely erroneous. Clearly, in order to obtain the best results, multiple measurements using different dies for each sample should be performed in order to rule out any potential artifacts.

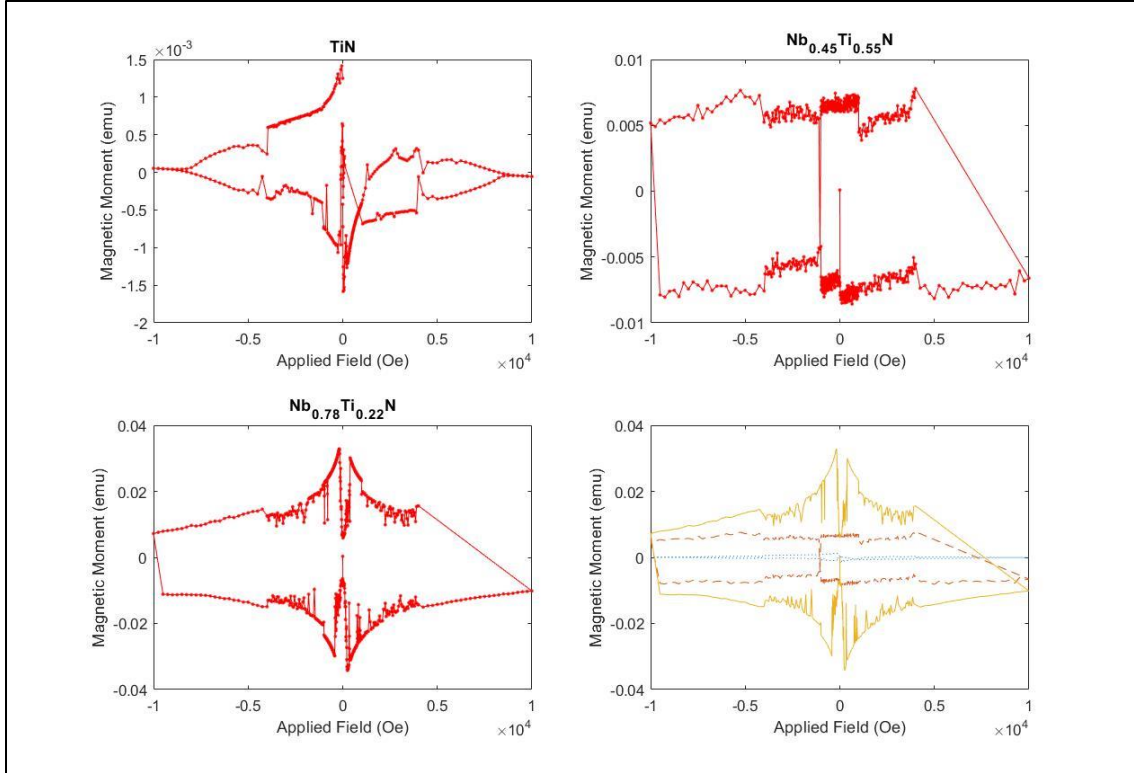


Figure 4-2 MPMS critical field measurements of the TiN , $\text{Nb}_{0.45}\text{Ti}_{0.55}\text{N}$, and $\text{Nb}_{0.78}\text{Ti}_{0.22}\text{N}$ films analyzed. Lower right graph shows the comparison between the three.

4.3 Critical Temperature Measurements

Using the same instrument, MPMS3, T_c measurements were done for our samples, except for Nb_2N given time considerations. The procedure consists of a thermal cycling under two conditions, zero field cooling (ZFC) and field cooling (FC). The first one implies the sample is first cooled to a $T < T_c$, 2 K in our case, without any applied field, the latter being the sample cooling while a small field is applied. The procedure is as follows. After the sample enters the MPMS3, it must first be centered, as to acquire the best possible measurements. For this, a 1000 Oe field is created with the restraint of “no overshoot”. This means that the field is slowly increased to 1000

Oe without passing above it. After this, the sample is passed through the detection coils and the MPMS3 analyzes the signal strength as a function of position, indicating the actual position of the sample within the chamber. The sample offset is then adjusted, and the field zeroed with overshoot allowed, lowering the field to zero and below (negative field) as to ensure that now fields remain in the detection coil prior to actual measurements; now the system is ready for T_c measurements. The first measurement is under ZFC conditions. The sample is cooled to 2 K at 0 field and then a small field (10 Oe) is applied, so its interaction with the sample can be measured. Then, the temperature is raised at rate of 0.35 K/min to above T_c , 20 or 30 K, concluding the ZFC measurement. While the field is maintained, the temperature is then lowered again to 2 K, this being the FC measurement.

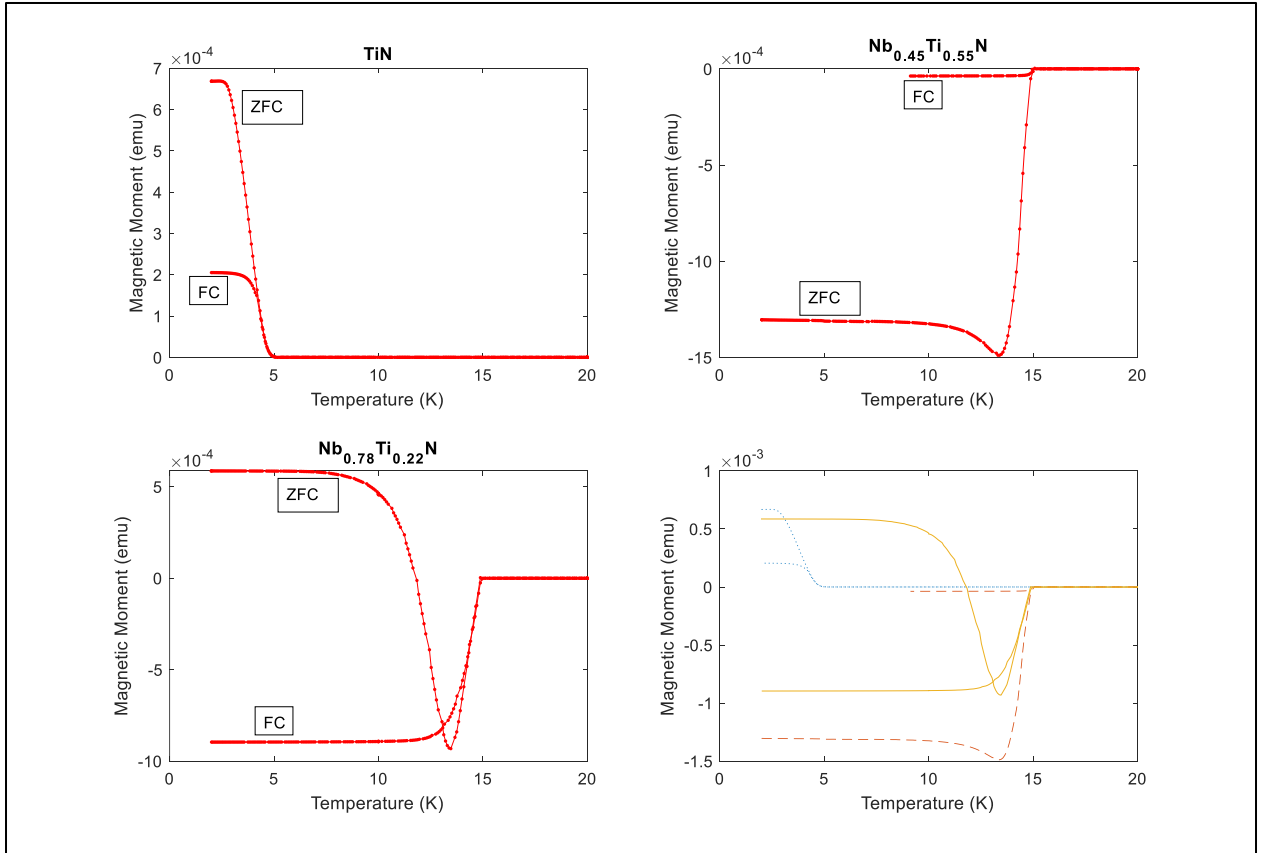


Figure 4 MPMS T_c measurements of the TiN, $Nb_{0.45}Ti_{0.55}N$, and $Nb_{0.78}Ti_{0.22}N$ films analyzed. The lower right graph shows the comparison between the three.

Figure 4-3 shows the T_c measurements for both ZFC and FC conditions of the different alloy films analyzed. From the MPMS data for TiN, the T_c was found to be 4.7 K under ZFC conditions and 4.7 K at FC conditions. For the $Nb_{0.45}Ti_{0.55}N$ sample, the T_c was 14.9 K and 14.9 K under ZFC and FC conditions, respectively. Finally, the $Nb_{0.78}Ti_{0.22}N$ sample exhibited a 15.1 K and 15.0 K at ZFC and FC conditions, respectively. The determination of the T_c from the data is straightforward, with the T_c being the temperature at which the magnetic moment signal becomes zero. As in the case of DC measurements, the repeatability of these measurements, having been made once, affects the uncertainty, which is unknown. In a physical sense, at this temperature, since superconductivity is lost, the shielding currents also vanish and thus the Meissner effect

is no longer observed. Thus, the magnetic field lines will penetrate the sample uniformly, so no magnetic moment signal is measured. There are, however, other peculiarities from the data figure that are worth discussing. The first one has to do with the TiN's magnetic moment magnitude. Ideally, a superconductor will show a negative magnetization signal when it is cooled under T_c , a key aspect of a diamagnet. In this case, however, the magnitude of the signal was positive, albeit the behavior is consistent with that of a superconductor. This fact might imply that perhaps the orientation of the applied field was opposite for this sample than for the rest.

The second has to do with both NbTiN samples' ZFC curves. They should, ideally, be similar to that of TiN in shape, less the opposite magnetization sign. The measurement starts from 2 K, and as temperature is risen, instead of observing the common behavior of magnetization dropping to zero from a negative value, instead we observe a dip, followed by a complete drop in magnetization. Moreover, the sample with highest Nb fraction starts with a positive magnetization, switching to a negative value as temperatures approach T_c , followed by the expected zeroing. It is unclear as to what may be causing this. Despite extensive literature research into the matter, no logical explanations seemed to arise. Given that, for each sample, only one measurement was made, it is possible that this unusual behavior be simply a measurement artifact. However, it is worth pointing out that the Nb source used to grow our samples was later found to have some Si contamination. Additionally, being thin films, only a small fraction of the total sample is the material of interest, the rest being the substrate (Al_2O_3) and a Ti backing layer. It is possible that under measurement conditions, the combination of these materials with the Si impurities could cause an

abnormal signal behavior. Despite all these possibilities, no cause can be isolated unless samples are remeasured or compared with samples lacking the Si contamination.

The third peculiarity, which is expected, is the difference between the ZFC and FC curves for all samples, in terms of magnitude of the signal. In all cases, the ZFC shows a higher signal magnitude compared with the FC one. This behavior demonstrates that all these samples are type-II superconductors. For a type-I superconductor, the curves should have very similar magnitudes, if not identical. However, due to flux pinning, the fraction of superconducting material is less, and thus the magnitude of the diamagnetic signal will be suppressed, as can be seen.

Chapter 5: Comparisons and Future Considerations

5.1 Significance and Result Summary

Throughout the literature one can find reports of films featuring the alloys presented in this thesis. Most of these, however, have been grown on different substrates, like MgO^{22,34,38}, which has been associated with higher losses³⁹, and Si^{35,38,40}. Although there are reports of films grown on sapphire^{22,41,42}, most of these describe films grown using sputtering deposition methods. Sputtering methods usually operate at higher chamber pressures, which could lead to film contamination unless extreme care and attention are given to the cleanliness of the system and materials. Additionally, the plasma employed for deposition can cause ion bombardment on the substrate, producing smaller grains than MBE as observed by the strength of the TiN XRD peaks⁴³. This is in contrast with molecular beam epitaxy, which operates at lower pressures, with precursors been generated either by effusion cells or electron guns.

Certainly, future research into this alloy system will lead to the exploration of different methods of film deposition. The work presented here helps narrow this knowledge gap by providing some preliminary work on MBE grown films from this alloy system. It is my hope that any future researcher that reads this work ends up, at least, having some idea of where the field stands and where to go from here. For the purposes of facilitating this information, I provide table 5-1 summarizing the essential findings in this work.

Table 2 Summary of results.

Compound	TiN	Nb _{0.45} Ti _{0.55} N	Nb _{0.78} Ti _{0.22} N	Nb ₂ N
Lattice Parameter a_c : (nm)	0.423	0.432	0.437	0.303
Film Thickness (nm)	45	205	88	37
RMS Roughness [2 μm / 10 μm] (nm)	1.16 / 1.35	8.84 / 9.85	1.72 / 1.76	4.33 / 5.22
T _c (K)	4.2	15.2	14.8	9.9
ΔT_c (K)	0.03 \pm 0.03	0.19 \pm 0.04	0.23 \pm 0.09	0.026 \pm 0.026
RRR	1.78	1.19	0.84	0.50
H _{c1} (Oe)	\sim 69.6	--	\sim 250	--
H _{c2} (Oe)	9 E3	--	>9 E3	--

5.2 Comparison Between Measurement Systems

We have used two different systems to analyze the superconducting properties of our samples, namely the MPMS3 magnetometer and our ADR system with the DC measurement tools. Although the operating principle of the instruments is completely different, some of the obtained information is the same, like the determination of T_c for our films. On this regard, the employment of two systems allowed for the confirmation of the obtained T_c values, with both methods providing very concurring results. The question arises then of, which of these tools is more convenient, or better, for our purposes. They're both essential, since there is not a complete overlap in terms of the obtained information. The MPMS3 provides us with both T_c and critical field measurements. It is very versatile in terms of range of operating conditions, being able to change sample temperature and applied field in minutes. Additionally, sample preparation, and switching, is facile, and the overall process isn't complicated and mostly automated. On the other hand, the ADR DC measurements provide resistivity information, which in turn gives us the RRR, allowing to have some insight into the

quality and behavior of the grown films. However, being a non-established instrument and more of a lab-developed method of analysis, it lacks versatility in some areas. One issue is the waiting time, with the system taking nearly 15 hours to achieve cryogenic temperatures. Once cold, there is no individual sample heating that can be made. Fortunately, there is the possibility of adding a heating element to individually change the temperature of the sample while keeping the rest of the system at a low temperature. Another issue is the more complicated sample preparation and the fact that only four samples can be placed into the ADR at a time. Despite this, the hands-on nature of the process makes it, at least to me, more interesting than the simplicity offered by the MPMS3. Finally, being our instrument, the ADR is always available, while the MPMS3, being a campus instrument, is very hard to get time on.

5.3 Future Work

An interesting aspect of research is that, it never ends. As data was obtained and analyzed, answers to the question “what’s next?” kept arising. Sadly, time limitations force these questions to remain as such, but also as invitations to whom may continue this work. At the time of this writing, cooldown data for TiN was still to be acquired, and is a simple first step into the continuation of this work. Additionally, the addition of a heating element into the ADR system will allow for more versatile and fast measurements of resistivity data of future samples. A lot of uncertainties remain regarding the MPMS3 measurements. A NbN sample, is yet to be measured using this instrument to obtain its T_c and critical field values. In addition to this information, insight into whether the dip observed in the MPMS3 T_c data was caused by

contamination of the Nb source used for sample growth. If the cause was indeed the contamination, a bigger dip could be expected, following the trend of intensifying dip with higher Nb content. Measurement of the substrate with and without the Ti back layer will allow to eliminate any substrate contributions to the observed magnetic moment behavior.

Additional measurements should be made for different dies of the same samples, since only one piece was measured for each sample. If all measurements for each sample concur, it can be ruled out that the cause was the measurement procedure. Another aspect of the T_c to be analyzed further is its variation with field intensity. A higher field is expected to suppress T_c . As observed in the critical field measurements, the $Nb_{0.45}Ti_{0.55}N$ sample data was not useful as it was severely poor in quality. Obtaining proper data will allow to observe any potential trends in critical field values as alloy fractions are varied. Finally, growth and analysis of more alloy fractions will provide more information and better resolution into the trends observed in the superconducting properties of the NbN-TiN alloy system.

Bibliography

- ¹ P.W. Shor, **26**, 1484 (1995).
- ² A. Gali, E. Janzén, P. Deák, G. Kresse, and E. Kaxiras, Phys. Rev. Lett. **103**, 1 (2009).
- ³ J.I. Cirac and P. Zoller, Phys. Rev. Lett. **74**, 4091 (1995).
- ⁴ S. Nadj-Perge, S.M. Frolov, E.P.A.M. Bakkers, and L.P. Kouwenhoven, Nature **468**, 1084 (2010).
- ⁵ J.R. Petta, A.C. Johnson, J.M. Taylor, E.A. Laird, A. Yacoby, M.D. Lukin, C.M. Marcus, M.P. Hanson, and A.C. Gossard, Science (80-.). **309**, 2180 (2005).
- ⁶ W.D. Oliver and P.B. Welander, MRS Bull. **38**, 816 (2013).
- ⁷ K.H. Bennemann and J.B. Ketterson, editors , *Superconductivity* (Springer Berlin Heidelberg, Berlin, Heidelberg, 2008).
- ⁸ M.H. Devoret and J.M. Martinis, Exp. Asp. Quantum Comput. **3**, 163 (2005).
- ⁹ F.M. Grosche, *Superconductivity*. (Springer Berlin Heidelberg, Berlin, Heidelberg, 2004).
- ¹⁰ W. Qiu, K. Makise, H. Terai, and Z. Wang, Phys. Procedia **36**, 360 (2012).
- ¹¹ C.P. Poole, R. Prozorov, H.A. Farach, and R.J. Creswick, *Properties of the Normal State* (2014).
- ¹² J. Bardeen, L.N. Cooper, and J.R. Schrieffer, Phys. Rev. **108**, 1175 (1957).
- ¹³ V.L. Ginzburg, Nuovo Cim. Ser. 10 **2**, 1234 (1955).
- ¹⁴ C. Kittel, *Introduction to Solid State Physics* (John Wiley & Sons, Incorporated, 2004).
- ¹⁵ I. Introduction and I. Brief, *Phenomenon of Superconductivity 2* (2014).

- ¹⁶ L.J. Zeng, S. Nik, T. Greibe, P. Krantz, C.M. Wilson, P. Delsing, and E. Olsson, J. Phys. D. Appl. Phys. **48**, (2015).
- ¹⁷ R. Lu, A.J. Elliot, L. Wille, B. Mao, S. Han, J.Z. Wu, J. Talvacchio, H.M. Schulze, R.M. Lewis, D.J. Ewing, H.F. Yu, G.M. Xue, and S.P. Zhao, IEEE Trans. Appl. Supercond. **23**, 1 (2013).
- ¹⁸ A.A. Bolzan, C. Fong, B.J. Kennedy, and C.J. Howard, J. Solid State Chem. **113**, 9 (1994).
- ¹⁹ A. Kafizas, C.J. Carmalt, and I.P. Parkin, Coord. Chem. Rev. **257**, 2073 (2013).
- ²⁰ V.K. Prokudina, in *Concise Encycl. Self-Propagating High-Temperature Synth.* (Elsevier, 2017), pp. 398–401.
- ²¹ H. Kashani, M. Heydarzadeh Sohi, and H. Kaypour, Mater. Sci. Eng. A **286**, 324 (2000).
- ²² A. Torgovkin, S. Chaudhuri, A. Ruhtinas, M. Lahtinen, T. Sajavaara, and I.J. Maasilta, Supercond. Sci. Technol. **31**, (2018).
- ²³ A. Torgovkin, S. Chaudhuri, J. Malm, T. Sajavaara, and I.J. Maasilta, IEEE Trans. Appl. Supercond. **25**, 1 (2015).
- ²⁴ M. Engineering and M. Science, *Synthesis and Characterization of Superconducting Thin Films* (2001).
- ²⁵ J.J. Olaya, L. Huerta, S.E. Rodil, and R. Escamilla, Thin Solid Films (2008).
- ²⁶ H. Oikawa, R. Akiyama, K. Kanazawa, S. Kuroda, I. Harayama, K. Nagashima, D. Sekiba, Y. Ashizawa, A. Tsukamoto, K. Nakagawa, and N. Ota, Thin Solid Films **574**, 110 (2015).
- ²⁷ C. Richardson, Christopher; Alexander, Ashish; Weddle, in *APS Meet. Abstr.*

(2019).

²⁸ V. Valvoda, J. Alloys Compd. **219**, 83 (1995).

²⁹ F. Mercier, S. Coindeau, S. Lay, A. Crisci, M. Benz, T. Encinas, R. Boichot, A. Mantoux, C. Jimenez, F. Weiss, and E. Blanquet, Surf. Coatings Technol. **260**, 126 (2014).

³⁰ Y. Krockenberger, S.I. Karimoto, H. Yamamoto, and K. Semba, J. Appl. Phys. **112**, (2012).

³¹ F. Lefloch, C. Hoffmann, and O. Demolliens, Phys. C Supercond. Its Appl. **319**, 258 (1999).

³² W. Spengler, R. Kaiser, A.N. Christensen, and G. Müller-Vogt, Phys. Rev. B **17**, 1095 (1978).

³³ J.R. Gavaler, D.W. Deis, J.K. Hulm, and C.K. Jones, Appl. Phys. Lett. **15**, 329 (1969).

³⁴ N.N. Losad, V. V. Roddatis, S.N. Polyakov, A. V. Varlashkin, B.D. Jackson, P.N. Dmitriva, J.R. Gao, and T.M. Klapwijk, IEEE Trans. Appl. Supercond. **11**, 3832 (2001).

³⁵ M. Cyberek, T. Farrahi, J. Lu, A. Kerr, R.M. Weikle, and A.W. Lichtenberger, IEEE Trans. Appl. Supercond. **29**, 1 (2019).

³⁶ S. Vishwanath, R. Yan, S. Katzer, N. Nepal, B. Downey, D. Meyer, G. ~B. ~S. Khalsa, J. Wright, Y. Han, D. Muller, A. Verma, E. Lochocki, K. Shen, H. ~G. Xing, and D. Jena, in *APS Meet. Abstr.* (2017), p. R41.009.

³⁷ O. Yildirim, Effect of Microstructure on the Magnetic Properties of Transition Metal Implanted TiO₂ Films, 2016.

- ³⁸ H. G.Leduc, J. W.kooi, and J. Zmuidzinas, Ninth Int. Symp. Sp. Terahertz Technol. 305 (1998).
- ³⁹ W. Qiu, K. Makise, H. Terai, Y. Nakamura, and Z. Wang, J. Phys. Conf. Ser. **507**, (2014).
- ⁴⁰ H. Akaike, K. Munemoto, Y. Sakakibara, and A. Fujimaki, IEEE Trans. Appl. Supercond. **29**, 1 (2019).
- ⁴¹ R. Barends, H.L. Hortensius, T. Zijlstra, J.J.A. Baselmans, S.J.C. Yates, J.R. Gao, and T.M. Klapwijk, IEEE Trans. Appl. Supercond. **19**, 936 (2009).
- ⁴² M. Guziewicz, A. Laszcz, J.Z. Domagala, K. Golaszewska, J. Ratajczak, R. Kruszka, M. Juchniewicz, A. Czerwinski, and W. Slysz, Electron Technol. Conf. 2013 **8902**, 89022S (2013).
- ⁴³ S. Ohya, B. Chiaro, A. Megrant, C. Neill, R. Barends, Y. Chen, J. Kelly, D. Low, J. Mutus, P.J.J. O'Malley, P. Roushan, D. Sank, A. Vainsencher, J. Wenner, T.C. White, Y. Yin, B.D. Schultz, C.J. Palmstrøm, B.A. Mazin, A.N. Cleland, and J.M. Martinis, Supercond. Sci. Technol. **27**, (2014).